

# 1 Size-differentiated Export <sup>c1</sup>Flux in Different 2 Dynamical Regimes in the Ocean

3 M. Dever<sup>1</sup>, D. Nicholson<sup>1</sup>, M. M. Omand<sup>2</sup>, and A. Mahadevan<sup>1</sup>

4 <sup>1</sup>Woods Hole Oceanographic Institution, Woods Hole, MA 02543, USA

5 <sup>2</sup>Graduate School of Oceanography, University of Rhode Island, Narragansett, Rhode Island, USA

## 6 Key Points:

- 7 Submesoscale dynamics enhance the contribution of slow-sinking particles to  
POC export, especially for steep particle size-spectrum slopes
- 8 Remineralization processes intensify the role of slow-sinking particles, to the  
point where these particle sometime dominate POC export

---

<sup>c1</sup> *Text added.*

11 **Abstract**

12 Export of Particulate Organic Carbon (POC) is mainly driven by gravitational sinking.  
 13 Thus, traditionally, it is thought that larger, faster-sinking particles make up most of  
 14 the POC export flux. However, this need not be the case <sup>c1</sup>for particles whose sinking  
 15 speeds are comparable to the vertical velocities of a dynamic oceanic flow field <sup>c2</sup>that  
 16 can influence the descent rate of particles. Particles with different settling speeds <sup>c3</sup>that  
 17 can be affected by the flow are released in two process-oriented model simulations of an  
 18 upper ocean eddying flow <sup>c4</sup>in the Northeast Pacific near Station Papa to evaluate the  
 19 impact of (1) ocean dynamics on the respective contribution of the different sinking-  
 20 velocity classes to POC export, and (2) the particle number size-spectrum slope. The  
 21 analysis reveals that the leading export mechanism changes from gravitationally-driven  
 22 to advectively-driven as submesoscale dynamics become more <sup>c5</sup>active in the region.  
 23 The vertical velocity associated with submesoscale dynamics enhances the contribution  
 24 of slower-sinking particles to POC export <sup>c6</sup>by a factor ranging from 3 to 10, espe-  
 25 cially where the relative abundance of small particles is large, as represented by a  
 26 steep particle size-spectrum slope. <sup>c7</sup>Remineralization <sup>c8</sup> generally decreases the total  
 27 amount of biomass exported, but its impact is weaker in dynamical regimes where  
 28 submesoscale dynamics are present and export is advectively-driven. <sup>c9</sup>In an advec-  
 29 tively-driven export regime, remineralization processes counter-intuitively enhance the  
 30 role of slower-sinking particles to the point where these slower-sinking velocity classes  
 31 dominate the export, therefore challenging the traditional paradigm for POC export.  
 32 This study demonstrates that slow-sinking particles can be a significant contribution,  
 33 and at times, even dominate the export flux.

34 **1 Introduction**

35 Photosynthesis in the sunlit upper ocean and the production of Particulate Or-  
 36 ganic Carbon (POC) takes up dissolved inorganic carbon and facilitates the uptake  
 37 of CO<sub>2</sub> from the atmosphere. The sinking of POC exports organic carbon from the  
 38 upper ocean to the interior, leading to the sequestration of carbon (Falkowski, Barber,  
 39 & Smetacek, 1998) on timescales ranging from days to years depending on the sinking  
 40 depth and circulation.

41 Traditionally, POC export is thought to occur through gravitational sinking and  
 42 one-dimensional models have been used to describe the sinking POC flux with depth.  
 43 Particles produced through primary and secondary production in the surface layer  
 44 that are relatively large and fast-sinking, tend to sink out of the upper surface layer  
 45 on timescales shorter than the timescale on which the particles get remineralized.  
 46 It is reasonable to treat POC export as sinking-dominated if the vertical advective  
 47 velocities in the ocean are weaker than the velocities associated with gravitational  
 48 sinking. However, Particulate Organic Matter (POM) has a wide range of particle  
 49 shape, size and type, that result in particle sinking velocities ranging from practically  
 50 zero, to several hundreds of meters per day. The size spectrum, or number distribution

---

<sup>c1</sup> in a dynamic oceanic flow field;

<sup>c2</sup> where the ocean velocity

<sup>c3</sup>

<sup>c4</sup>

<sup>c5</sup> important

<sup>c6</sup> A steeper particle size spectrum, also increases the relative contribution of smaller, slower-sinking particles

<sup>c7</sup> Implementing a r

<sup>c8</sup> scheme

<sup>c9</sup> Under specific conditions

of particle sizes, is usually characterized by a power law with the power ranging between -2 and -4, for which the abundance of small particles is  $\mathcal{O}(10^4 – 10^8)$  greater than large particles. The biomass size spectrum, which indicates the distribution of biomass vs. particle size, tends to be flatter and variable in shape (Sheldon, Prakash, & Sutcliffe, 1972) compared to the particle number spectrum, because the volume (and mass) of a particle scales with its linear size raised to a power that exceeds 1 (and typically varies between 2 and 3 depending on shape and porosity). Importantly, it means that a significant fraction of the particulate biomass is in the small size fraction. Even though the sinking velocity  $w_s$  of particles does not perfectly relate to particle size  $l$ , it is fair to assume that  $w_s \sim l^n$  (with  $n = 2$  according to Stokes law, and  $1 < n < 2$  for complex particle shapes). Due to this, as well as the fact that particles of organic matter are not very much greater in their densities than seawater, a significant fraction of the biomass sinks very slowly (at velocities less than tens of meters per day). When the gravitational sinking velocity of particles is comparable to (or smaller than) the vertical velocities in the flow field, the dynamics of the flow field can impact the trajectories and fate of the POC. Thus, depending on the flow dynamics, and the fraction of slow-sinking particulate biomass, the sinking of organic matter can be affected by the fluid flow in the ocean.

Recent studies have shown that ocean dynamics can play a role in driving the transport of carbon from the euphotic layer to the ocean interior. For example, enhanced vertical velocities along the edge of a mesoscale eddy led to a funneling of particles along the eddy's periphery (van Haren, Millot, & Taupier-Letage, 2006; Waite et al., 2016). Omand et al. (2015) found that submesoscale mixed layer eddies, while contributing to the restratification of a frontal zone, were subducting a large amount of non-sinking POC from the surface productive layer during the onset of the Spring bloom in the subpolar North Atlantic. Advectively subducting plumes or filaments of high oxygen, chlorophyll and small POC (evidenced through backscatter) were detected from a suite of gliders during the North Atlantic Bloom experiment (Alkire et al., 2012). Using model simulations to capture the process of eddy-driven subduction, Omand et al. (2015) estimated the downward advective flux of non-sinking POC and parameterized it. Briggs et al. (2011) quantified the flux of fast-sinking particles consisting largely of diatoms from observations of optical backscatter. But, these estimates did not account for a range of sinking particle velocities. Typically, particulate organic matter (POM) has a wide spectrum of sinking velocities and in order to understand its fate and export, we need to consider the biomass distribution as a function of the particle sinking velocity spectrum and its interaction with the dynamics of the flow field in the ocean.

A growing body of literature focusing on submesoscale (1-10 km) dynamics is exploring its impact on biogeochemical processes (Lévy, Ferrari, Franks, Martin, & Rivière, 2012; Mahadevan, 2016). Submesoscale dynamics, characterized by Rossby numbers of order 1, typically develop in filaments in areas where sharp density fronts exist (Klein & Lapeyre, 2009; McWilliams, 2016; Thomas, Taylor, Ferrari, & Joyce, 2013). In this dynamical regime, geostrophic balance breaks down and a secondary ageostrophic circulation develops across the front, capable of generating large vertical velocities on the order of 100 m/day (Fox-Kemper, Ferrari, & Hallberg, 2008; Mahadevan, 2016). On the denser side of the front, the vorticity is cyclonic and associated with downwelling velocities, while anticyclonic vorticity and upwelling is expected on the lighter side of the front. The distribution of relative vorticity across a front is asymmetric and skewed toward cyclonic vorticity (Rudnick, 2001), leading to more localized and more intense downwelling regions, as opposed to weaker and larger upwelling regions (Mahadevan & Tandon, 2006). Enhanced vertical velocities can generate a local bloom by supplying nutrients to the sunlit layer of the ocean (Lévy, Klein, & Treguier, 2001; Mahadevan & Archer, 2000), or can significantly increase the export of POC to

104 the ocean interior through downwelling (Estapa et al., 2015; Gruber et al., 2011; Lévy  
 105 et al., 2012; Omard et al., 2015).

106 The downwelling velocities  $\mathcal{O}(100 \text{ m/day})$  generated at submeso-scales provide  
 107 a physical mechanism capable of competing with gravitational sinking and thus ex-  
 108 porting particles over a larger portion of the particle size spectrum. Through this  
 109 mechanism, smaller particles can be exported on timescales shorter than their remi-  
 110 neralization timescales, despite their slower sinking velocities. Depending on the frac-  
 111 tion of biomass in smaller particles (i.e., with slow sinking velocities), the impact of  
 112 submesoscale dynamics on the export of POC is potentially significant.

113 In this study, we account for a range of particle sinking velocities in a dynamic  
 114 flow field. Despite progress on sampling and viewing particles in the ocean (McDonnell  
 115 & Buesseler, 2010), direct measurements of particles sinking velocities are difficult  
 116 to obtain, and often inferred from key parameters such as particle type, size, and  
 117 density. Though we acknowledge a large variability in these relationships, we assume  
 118 a relationship between particle size, biomass, and particle sinking velocity in order to  
 119 assess the impact of the flow dynamics and particle size spectrum on the export flux.

120 We rely on a submesoscale-resolving, non-hydrostatic ocean model to simulate the  
 121 dynamics in the upper few hundred meters of the ocean. The model does not represent  
 122 surface waves or boundary layer turbulence, but rather, examines the fate of particulate  
 123 organic matter beneath the turbulent surface boundary layer. The dynamical model  
 124 is coupled with a particle-tracking module to model the advection of particles by fluid  
 125 flow, while neglecting the effects of particle inertia and drag on their advection. In  
 126 addition, the particles sink with a range of sinking velocities (between  $0.025\text{--}5 \text{ m}$   
 127  $\text{day}^{-1}$ ) <sup>c1</sup>scaled from the range of vertical currents modeled in this region. We aim  
 128 to address the transitional regime of the particle sinking velocity spectrum, where  
 129 both advection and sinking speeds have similar order of magnitudes. This transitional  
 130 regime will thus vary depending on the local dynamics: in strong frontal regions such  
 131 as western boundary current, vertical currents can  $\mathcal{O}(100 \text{ m/day})$ .

132 The model is used to quantify the contribution of slow-sinking particles to carbon  
 133 export, as a function of (1) the dynamics of the flow field, (2) the slope of the sinking  
 134 velocity spectrum, and (3) the remineralization timescale. Particles in the model  
 135 are prescribed with both a constant and time-varying sinking velocity to mimic a  
 136 remineralizing behavior. Particles are released in two fundamentally different flow  
 137 fields in terms of dynamics based on observed conditions in the Northeast Pacific:  
 138 In the summer, where ocean dynamics are characterized by low Rossby numbers and  
 139 weak vertical advective velocities, and in the winter, where ocean dynamics include  
 140 submesoscale frontal structures and local Rossby numbers  $\mathcal{O}(1)$ . Both simulations  
 141 and the particle-tracking module are described in Section 2. The impact of particles  
 142 characteristics and ocean dynamics on the export of POC is quantified in Section 3,  
 143 and discussed in Section 4. Section 5 summarizes the key conclusions of the study.

## 144 2 Methods

### 145 2.1 Model setup and domain

146 This study uses a non-hydrostatic, three-dimensional, Process Study Ocean Model  
 147 (PSOM; Mahadevan, Olinger, & Street, 1996a, 1996b) to simulate an eddy field that is  
 148 representative of the Northeast Pacific Ocean. The model is set in a channel configura-  
 149 tion with periodic east-west boundaries, and solid boundaries in the south and north.  
 150 The domain covers 112 km in the x-direction, 304 km in the y-direction, and 1000 m

---

<sup>c1</sup> *Text added.*

in the vertical (Figure 1). The horizontal resolution is 500 m, while a stretched grid is used in the vertical with 32 levels ranging in thickness from 1.25 m near the surface to 70 m at the lowermost level. The model is integrated numerically in time and evolves the temperature, salinity, free-surface height, pressure, and three-dimensional velocity field from an initial state, subject to momentum and buoyancy fluxes applied through the surface boundary.

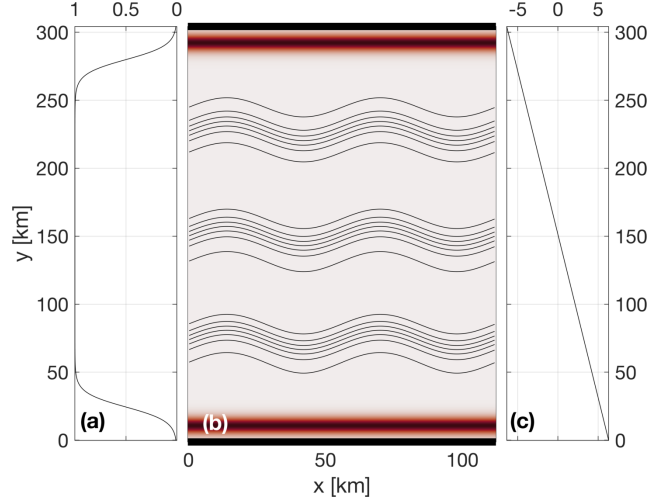


**Figure 1.** PSOM model setup. (a) Meridional profile of scaling coefficient that multiplies the time-varying zonal wind stress  $\tau_x$  shown in Fig. 3a. The taper at north and south boundaries prevents ‘coastal’ up-/down-welling being entirely concentrated in the boundary grid cell. (b) Restoration factor (color shading) used to dampen internal wave reflection at boundaries as well as up-/down-welling due to the windstress curl. Surface density contours (black) show the three fronts used to initialize the model. (c) Meridional variation of the time-dependent surface heat flux (Fig. 3a) prescribed over the domain.

Time-varying wind stress and heat flux are prescribed at the surface boundary. Time series are computed from measurements collected at Station Papa and available through the Pacific Marine Environmental Laboratory (PMEL, 2018). Daily wind stress and net heat fluxes are calculated over the period 2007-2016 to produce a year-long climatology. A squared low-pass filter with a cut-off frequency of 8.5 days is applied to both time series to remove high-frequency variability. In all numerical experiments, simulations are run for the first 5 days without any forcing applied to the surface boundary. Surface wind stress and heat fluxes are then linearly ramped up between days 5 and 10 of the simulation, to reach realistic values at day 10.

While the meridional component,  $\tau_y$ , is set to zero, the zonal component of the wind stress,  $\tau_x$ , is prescribed at the surface throughout the model domain and is tapered at the northern and southern boundaries to avoid excessive Ekman-driven upwelling and downwelling (Figure 1a). A restoration timescale is prescribed to contain the curl-driven upwelling and downwelling regions generated by the tapering of the wind stress, as well as to limit internal wave reflection at the solid boundaries back into the domain (Figure 1b). While net surface heat fluxes are homogeneous in the zonal direction, a meridional gradient is maintained throughout the simulation. The meridional gradient was determined from the North American Regional Reanalysis (NARR) product (Mesinger et al., 2006), and set to  $1/24 \text{ W/m}^2/\text{km}$  (Figure 1c).

Initial hydrographic conditions are determined from a three-dimensional gridded field of temperature and salinity from Argo floats (Gaillard, 2015; Gaillard, Reynaud, Thierry, Kolodziejczyk, & von Schuckmann, 2016). Argo data is averaged monthly over the period 2002-2012 and two different months are used to initialize the two main numerical experiments for this study: Climatological conditions in April are used to initialize the *Papa\_summer* experiment, while January climatological conditions are used to initialize the *Papa\_winter* experiment (Table 1). The north-south background density gradient is then intensified into three fronts located at  $y = 75$ ,  $y = 150$ , and  $y = 225$  km (Figure 1). The amplitude of the density gradient associated with the three fronts is determined from the probability distribution function (PDF) of the density gradients measured by underwater gliders deployed around Station Papa over the period 2008-2010 (Pelland, 2018; Pelland, Eriksen, & Cronin, 2016). To reduce model spin-up time, density fronts are perturbed by a sinusoidal wave with a wavelength close to the 1st baroclinic deformation radius ( $\lambda = 66$  km). Similar PSOM configurations were successfully used in previous studies (Mahadevan, D'Asaro, Lee, & Perry, 2012; Omand et al., 2015).

Two main experiments are conducted using the same configuration of PSOM, where only initial conditions and surface forcings are varied: *Papa\_summer* aims at generating ocean dynamics representing conditions in the Northeast Pacific in the summertime. Summer ocean dynamics are characterized by a flow generally in geostrophic balance, with relatively weak density gradients and low Rossby numbers ( $\ll 1$ ). *Papa\_winter* aims at capturing wintertime ocean conditions in the region. A different dynamical regime is expected to dominate during wintertime when mixed layers are deeper and lateral density gradients enhanced, with sharper density fronts, filament-like features and localized Rossby number  $\mathcal{O}(1)$  over spatial scales  $\mathcal{O}(1 \text{ km})$  (Callies, Ferrari, Klymak, & Gula, 2015; Mensa et al., 2013; Thompson et al., 2016). The individual characteristics of each of *Papa\_summer* and *Papa\_winter* are detailed below.

### **2.1.1 *Papa\_summer* Model Experiment**

In *Papa\_summer*, PSOM is initialized based on climatological Argo data in April. The magnitude of the density gradient across the front is set to  $3.34 \times 10^{-6} \text{ kg/m}^3/\text{m}$ , which corresponds to the 95<sup>th</sup> percentile of the PDF of density gradients measured in April from glider data collected in the region (Figure 2 and Table 1). The model is run with a timestep of 216 s and is allowed to spin-up for 60 days, allowing summer stratification to develop. The model is then run for 30 additional days, saving instantaneous model fields every 3 hours for particle tracking. The month of April is chosen for initialization so the experiment would capture the onset of positive net heat fluxes, and the summer restratification that ensues in July-August (Figure 2). In this region, the summer stratification is associated with large primary productivity, particle production, and POC export (e.g., fecal pellets, dead phytoplankton; Plant et al., 2016).

### **2.1.2 *Papa\_winter* Model Experiment**

In *Papa\_winter*, PSOM is initialized based on climatological Argo data in January. The frontal gradient is set to  $3.54 \times 10^{-5} \text{ kg/m}^3/\text{m}$ , which corresponds to the 99<sup>th</sup> percentile of the PDF of density gradients measured in January from glider data collected in the region (Figure 3 and Table 1). The model is allowed to spin-up for 50 days allowing for the prescribed fronts to become unstable. To accommodate for the larger density gradients and stronger velocities, the advective timestep is shortened to 108 s and the horizontal diffusivity is lowered to 0.2 m<sup>2</sup>/s throughout the experiment. The model is run for 30 additional days, saving instantaneous model fields every 1.5 hours for particle tracking. The month of January is chosen for initialization so the

224 **Table 1.** Summary of the key characteristics of PSOM experiments *Papa-summer* and  
 225 *Papa-winter*.

	<i>Papa-summer</i>	<i>Papa-winter</i>
Time period	April – July	January – March
Spin-up	60 days	50 days
Advective timestep	216 s	108 s
Horizontal diffusivity	1 m <sup>2</sup> s <sup>-1</sup>	0.2 m <sup>2</sup> s <sup>-1</sup>
Restoration timescale	3 days	15 days
Zonal wind stress	0 – +0.16 N m <sup>-2</sup>	-0.05 – +0.17 N m <sup>-2</sup>
Surface heat flux	-46.8 – +167.5 W m <sup>-2</sup>	-57.6 – +15.3 W m <sup>-2</sup>
Maximum M <sup>2</sup> ( $\times 10^{-8}$ )		
initial	3.2 s <sup>-2</sup>	33.9 s <sup>-2</sup>
spun-up	12.0 s <sup>-2</sup>	50.0 s <sup>-2</sup>
Maximum N <sup>2</sup> ( $\times 10^{-4}$ )		
initial	1.5 s <sup>-2</sup>	1.6 s <sup>-2</sup>
spun-up	3.1 s <sup>-2</sup>	1.1 s <sup>-2</sup>
Averaged mixed layer depth		
initial	73 m	85 m
spun-up	11 m	93 m

245 experiment would capture the time of year where the mixed layer is the deepest, and  
 246 Rossby number O(1) occur more frequently. The objective is for this experiment to  
 247 contrast *Papa-summer* by capturing the statistics of ocean conditions dominated by  
 248 submesoscale dynamics.

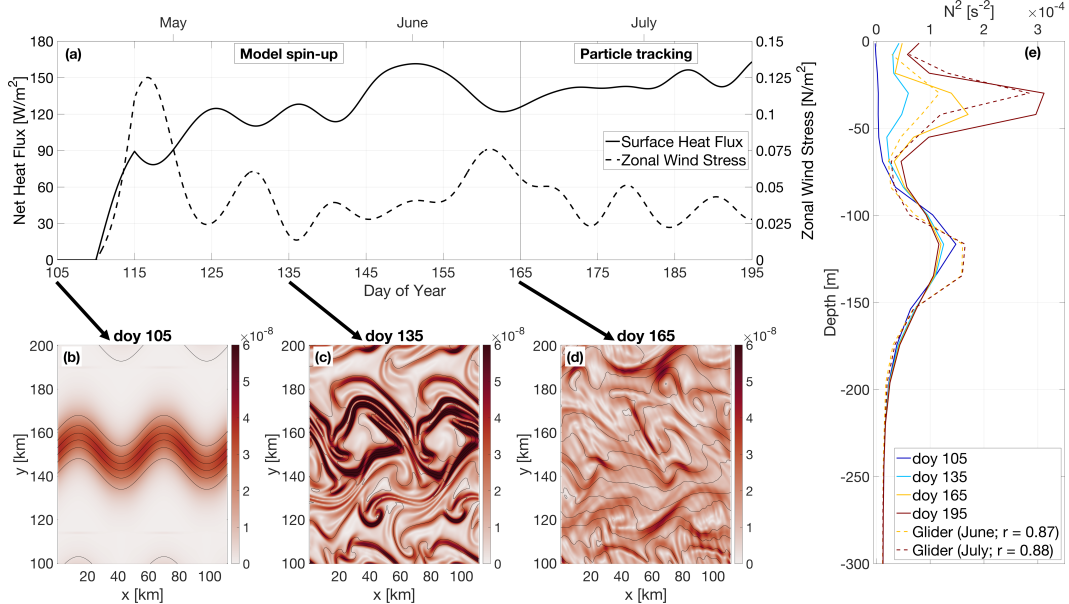
### 2.1.3 Validation

258 To ensure that PSOM simulations yielded realistic conditions for both *Papa-summer*  
 259 and *Papa-winter*, distributions of horizontal ( $M^2$ ) and vertical ( $N^2$ ) buoyancy gradi-  
 260 ents are compared with glider observations collected over the period 2008-2009 (Pelland  
 261 et al., 2016). During this period, underwater gliders sampled in a “bow-tie” pattern  
 262 centered on Station Papa. Gliders sample the water column in a triangular wave  
 263 pattern, whose shape is easily affected by currents, due to the slow moving speed of  
 264 the glider ( $\sim 1$  km/hr). It is therefore challenging to associate a specific spatial scale  
 265 with gradients computed between glider profiles, as profile separation distances can be  
 266 highly variable through depth and time. To circumvent this issue, horizontal buoy-  
 267 ancy gradients are computed between each pair of glider profiles available within one  
 268 branch of the bow-tie. Each along-track lateral buoyancy gradient is thus associated  
 269 with a specific separation scale and a timestamp. Glider-based density gradients can  
 270 be affected by internal waves. To filter the impact of internal waves on the PDF of  
 271 horizontal buoyancy gradients, only gradients computed at a scale of twice the Rossby  
 272 radius  $\pm 1$  km are considered. Rossby radii are estimated from the glider data and  
 273 are  $\sim 8$  km in winter and  $\sim 20$  km in summer.

## 2.2 Particle Tracking Experiments

### 2.2.1 Particle Advection Scheme

274 To quantify the impact of submesoscale dynamics on the export of Particulate  
 275 Organic Matter (POC), Lagrangian particle trajectories are computed using the same  
 scheme as in “TRACMASS” (Döös, Kjellsson, & Jönsson, 2013) with the flow fields



226 **Figure 2.** PSOM configuration for *Papa\_summer*. (a) Time series of net heat fluxes and wind  
 227 stress prescribed at the surface. Notice the positive heat fluxes, as well as downfront winds (i.e.  
 228 eastward) persisting throughout the experiment. (b)-(d) surface horizontal buoyancy gradients  
 229  $M^2 = |\nabla_H b|^2$  (in  $s^{-2}$ ) at day of year (doy) 105, 135, and 165. Black contours show isopycnals (in  
 230 kg/m<sup>3</sup>; CI = 0.01 kg/m<sup>3</sup>). (e) Vertical profile of the buoyancy frequency  $N^2$  at day of year 105,  
 231 135, 165, and 195, showing the development of summer stratification centered at  $z = 30$  m (solid  
 232 lines). Monthly-average vertical stratification obtained from glider profiles collected in June and  
 233 July are superimposed (dashed lines), along with the correlation coefficient between observations  
 234 and model outputs.

from the two experiments described above. The three-dimensional, non-divergent velocity components from the faces of each “C” grid cell are linearly interpolated onto the particle’s position within the grid cell. For example, the eastward (along the x-axis) velocity of a particle is given by

$$u(x) = u_{i-1} + \frac{(x - x_{i-1})}{(x_i - x_{i-1})}(u_i - u_{i-1}), \quad (1)$$

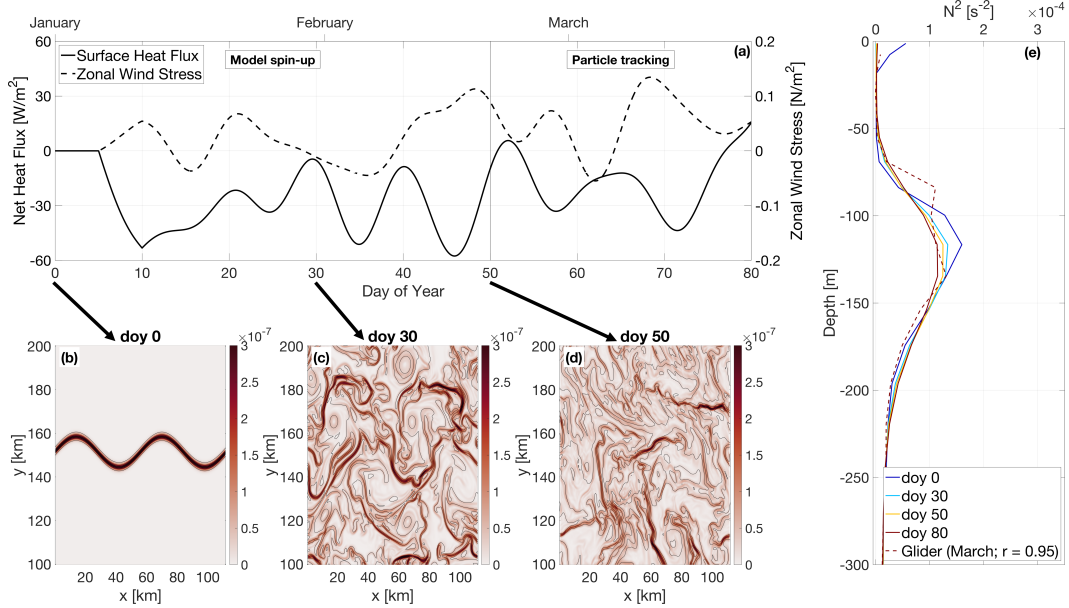
where the subscripts  $i - 1$  and  $i$  denote the western and eastern walls of the grid cell where the particle is located, respectively. This can be re-written as

$$\frac{\partial x}{\partial t} + \beta x + \delta = 0, \quad (2)$$

where  $\beta = (u_i - u_{i-1})/\Delta x$  and  $\delta = -u_{i-1} - \beta x_{i-1}$  (Döös et al., 2013). This differential equation can be solved analytically for  $\beta \neq 0$  as

$$x_{t_1} = \left( x_0 + \frac{\delta}{\beta} \right) \exp^{-\beta(t_1 - t_0)} - \frac{\delta}{\beta} \quad (3)$$

The time it will take for the particle to reach the eastern or western face of the grid cell can be computed by taking  $x_{t_1} = x_i$  or  $x_{t_1} = x_{i-1}$ , respectively, and solving for  $t_1$ . For each advective timestep, the times required for the particle to reach any of the 6 walls of the grid cell are computed using (3). If any of those times is shorter than the advective timestep, the particle is advected until it reaches the cell wall. Then the flow field in the adjacent grid cell is considered and the particle is advected over the remaining time.



249 **Figure 3.** PSOM configuration for *Papa\_winter*. (a) time series of net heat fluxes and wind  
 250 stress prescribed at the surface. Notice the mostly negative heat fluxes, as well as alternating  
 251 zonal wind direction. (b)-(d) surface horizontal buoyancy gradients  $M^2 = |\nabla_H b|^2$  (in  $s^{-2}$ ) at day  
 252 of year (doy) 0, 30, and 50. Black contours show isopycnals (in  $kg/m^3$ ; CI =  $0.01\ kg/m^3$ ). (e)  
 253 Vertical profile of the buoyancy frequency  $N^2$  at doy 0, 30, 50, and 80, showing the persistence  
 254 of the halocline between  $z = 80$  and  $z = 180$  m throughout the experiment (solid lines). Monthly-  
 255 average vertical stratification obtained from glider profiles collected in March is superimposed  
 256 (dashed line), along with the correlation coefficient between observations and model outputs.

### 283 2.2.2 Particle Seeding

284 For all particle-tracking experiments, a single particle seeding event is prescribed.  
 285 In the horizontal, particles are seeded every 250 m over the entire domain in the x-  
 286 direction, and for  $100 < y < 200$  km in the y-direction. The seeding is centered over  
 287 the mean position of the central front (see Figure 2) and is therefore not affected by  
 288 undesired effects created by the solid north-south solid boundaries. In the vertical,  
 289 particles are seeded every 1 m between 75 and 85 m. This depth range is chosen as it  
 290 corresponds to the average euphotic depth at Station Papa, defined by the 1% light  
 291 level. <sup>c1</sup>Particle seeding is located at the base of the euphotic layer where biological  
 292 processes not captured by the particles (e.g., grazing, repackaging, aggregation,  
 293 etc.) are not as active (Ducklow, Steinberg, & Buesseler, 2001). The euphotic depth  
 294 was computed for the months of February and June over the period 2007-2016 from  
 295 profiles of Photosynthetically <sup>c2</sup>Active Radiation (PAR) collected at Station Papa as  
 296 part of the long-term monitoring of Line P executed by the Department of Fisheries  
 297 and Ocean Canada<sup>c2</sup>. The average euphotic depth computed for both of these months  
 298 is around 80 m, which agrees with previously established estimates of the euphotic  
 299 depth (Harrison, Whitney, Tsuda, Saito, & Tadokoro, 2004; Sherry, Boyd, Sugimoto,  
 300 & Harrison, 1999).

<sup>c1</sup> *Text added.*

<sup>c2</sup> *Available*

<sup>c2</sup> <https://www.waterproperties.ca/linep/index.php>

301 In each particle-tracking experiment, four different classes of particles are re-  
 302 leased. Each particle class is characterized by a different sinking velocity: 0.025, <sup>c3</sup>1,  
 303 and 5 m/day. <sup>c4</sup>In this study, these particle classes are referred to as slow-, intermediate-, and fast-sinking particles. This characterization is not based on the absolute  
 304 value of the sinking rate, but rather on the ratio with vertical currents in the study  
 305 region. While 5 m/day remains a relatively slow sinking rate, the slowest-sinking class  
 306 is essentially selected to represent non-sinking particles: based on the setup of our ex-  
 307 periments, the slowest-sinking particles would take 800 days on average to be exported  
 308 to a depth of 100 m through gravitational sinking, a timescale much greater than com-  
 309 monly observed remineralization timescales. The fastest-sinking velocity is chosen as  
 310 an end-member velocity class of particle<sup>c5</sup>, based on the PDF of vertical velocities in  
 311 the model. At any given time, at least 85% of the model vertical velocity is weaker  
 312 than 5 m/day. The results presented for the 5 m/day sinking class can therefore be  
 313 theoretically extrapolated to any class with a higher sinking velocity.

315 The advective timestep for particles is set to 1.5 hours. The flow field is linearly  
 316 interpolated in time between model outputs, justifying the higher temporal resolution  
 317 used for particle tracking in *Papa\_winter*. Particle positions are saved every 3 hours,  
 318 along with key model variables interpolated onto the particle positions (e.g., density,  
 319 vorticity). Particles are tracked for <sup>c1</sup>four weeks (28 days). Each particle-tracking ex-  
 320 periment contains 1,971,717 particles per sinking-velocity class, for a total of 9,858,585  
 321 particles. Particles located deeper than the maximum winter mixed layer (i.e., 100 m;  
 322 Pelland et al., 2016; Plant et al., 2016) are considered exported, as they will likely not  
 323 be re-entrained into the mixed layer.

### 324 **2.2.3 Density and Biomass Spectra**

325 <sup>c2</sup>To quantify vertical export fluxes, both the distribution of the number of par-  
 326 ticles and the associated biomass can be modeled based on two main variables: the  
 327 particles' radii and the rate at which the number of particles changes with respect to  
 328 the size. The particle number is modeled using a power-law function as a function of  
 329 size that is driven by the parameter  $\xi$ . This slope  $\xi$  of the size spectrum of particles  
 330 (also known as the Junge slope; White et al., 2015) is the slope of the log-log curve of  
 331 particle number  $N$  vs. particle radius  $r$ , where

$$N(r) = N_0 \left( \frac{r}{r_0} \right)^{-\xi}. \quad (4)$$

325 Here,  $N_0$  and  $r_0$  represent a reference particle number and radius, chosen arbitrarily.  
 326 <sup>c3</sup>Typical values for  $\xi$  derived from both in-situ observations and satellite data have  
 327 been reported to range from 3 to 6 (Kostadinov, Siegel, & Maritorena, 2009; White et  
 328 al., 2015, Z. Xiaodong, personal communication). For small particles ( $<400 \mu\text{m}$ ) and  
 329 relatively low temperature ( $<15^\circ\text{C}$ ), it has been shown that the relationship between  
 330 particle radius  $r$  and sinking velocity  $w_s$  exhibits a range of variation and is difficult  
 331 to determine empirically. Nevertheless, Stokes' law, where  $w_s \propto r^2$ , is often used as a  
 332 lower-bound sinking velocity estimate (Bach et al., 2012).

<sup>c3</sup> 0.05,

<sup>c4</sup> Text added.

<sup>c5</sup> that will be exported in its entirety over the course of our experiment.

<sup>c1</sup> three

<sup>c2</sup> Text added.

<sup>c3</sup> Text added.

Assuming a Stokes-like relationship, we can construct based on (4) a particle sinking velocity spectrum  $N(w_s)$ , as <sup>c4</sup>a function of the Junge slope  $\xi$ :

$$N(w_s) = N_0 \left( \frac{w_s}{w_{s_0}} \right)^{-\xi/2}, \quad (5)$$

where  $w_{s_0}$  is the sinking speed of particles with radius  $r_0$ . For a specific slope and sinking-velocity class, an equivalent number of particles per simulated particle can be computed using (5) (See Figure 4). For example, using the largest sinking velocity class as a reference (i.e.,  $w_{s_0} = 5$  m/day and  $N_0 = 1,971,717$ ), and a spectral slope  $\xi = 4$ , each simulated particle with a sinking velocity of 0.025 m/day in fact represents 40,000 particles (Figure 4). The relative biomass of a particle in a specific sinking-velocity class,  $B_p(w_s)$  can be estimated if the biomass is assumed to scale with the particle's volume. The relative biomass of one particle in a sinking-velocity class  $w_s$  can therefore be computed as

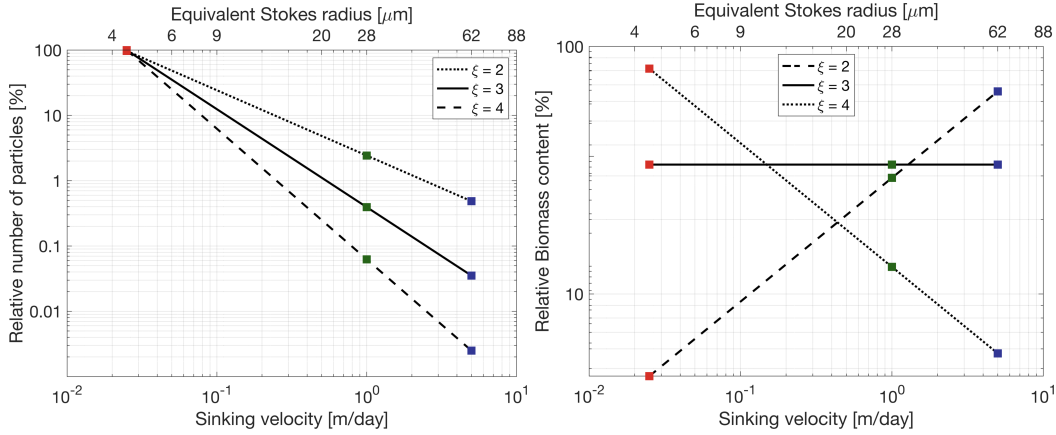


**Figure 4.** Relative number of particles (left) and biomass (right) as a function of sinking velocity  $w_s$ . Sinking velocity spectrum are shown for three different Junge slope  $\xi$ : 2 (dotted), 3 (solid), and 2 (dashed). Colored squares indicate the sinking velocities of the three particle classes modeled: 0.025 m/day (red), 1 m/day (green), and 5 m/day (blue).

$$B_p(w_s) = B_p(w_{s_0}) \left( \frac{w_s}{w_{s_0}} \right)^{3/2} \quad (6)$$

where  $B_p(w_{s_0})$  is the biomass of a particle in the sinking velocity class  $w_{s_0}$ . The total biomass associated with one simulated particle can be obtained by scaling (6) by the ratio  $N(w_s)/N_0$ :

$$B(w_s) = B_0 \left( \frac{w_s}{w_{s_0}} \right)^{3/2} \frac{N(w_s)}{N_0} \quad (7)$$

where  $B_0 = B_p(w_{s_0})$ . Combining (5) and (7) yields an expression relating the biomass associated with a simulated particle for a specific sinking-velocity class and the spectral slope (Figure 4):

$$B(w_s) = B_0 \left( \frac{w_s}{w_{s_0}} \right)^{\frac{3-\xi}{2}}. \quad (8)$$

---

<sup>c4</sup> *Text added.*

Using the same example as before where  $\xi = 4$ , if the amount of biomass associated with one simulated particle in the 5 m/day sinking-velocity class is taken as  $B_0 = 1$ , then one simulated particle sinking at 0.025 m/day contains 14.14 units of biomass and a single particle contains  $14.14/40,000 = 3.5 \times 10^{-4}$  units of biomass (see Figure 4). This normalized formulation of particle number and biomass (see Equations (5) and (8)) has the advantage that the impact of spectral slope on the relative export of biomass can be quantified without needing a large number of particle-tracking experiments, where the number of seeded particles would vary to account for the different spectral slopes. For the purpose of this study, only the relative amount of biomass is relevant. For simplicity, we define a normalized biomass unit for  $\xi = 3$  as  $B_0 = 1$ . The values taken by  $B_0$  for other Junge slopes  $\xi$  are computed under the condition that the total amount of biomass is kept constant (Figure 4b).

#### 2.2.4 Particle Remineralization Scheme

Remineralization of particles as they sink through the water column impacts the amount of biomass exported. Slow-sinking particles generally contain less biomass and spend more time in the mixed layer, which means that they are remineralized at a shallower depth than faster sinking particles. Remineralization processes are complex, species-dependent, and generally not well-understood. In the absence of a consensus on a general functional form of particle remineralization, we rely on an idealized relationship which assumes that the biomass content of a particle decreases in time proportionally to the particle volume. Remineralization is thus modeled as an exponential decrease of biomass with time at a rate  $k$  (Iversen & Ploug, 2010, 2013)

$$B(t) = B^0 \exp(-kt), \quad (9)$$

where  $B^0$  denotes the biomass content at  $t = 0$  days, and the remineralization rate is taken to be  $k = 0.13 \text{ day}^{-1}$  in this study (Iversen & Ploug, 2010). This remineralization rate is independent of particle sinking velocity, and seems to lie within the range of other estimates (Iversen & Ploug, 2010, 2013; Ploug, Iversen, Koski, & Buitenhuis, 2008). The change in biomass with time is in turn expected to affect the sinking velocity of the particle. Given that  $B \propto w^{3/2}$  (see Equation (6)), particles in all sinking-velocity classes undergo a decay in sinking speed according to

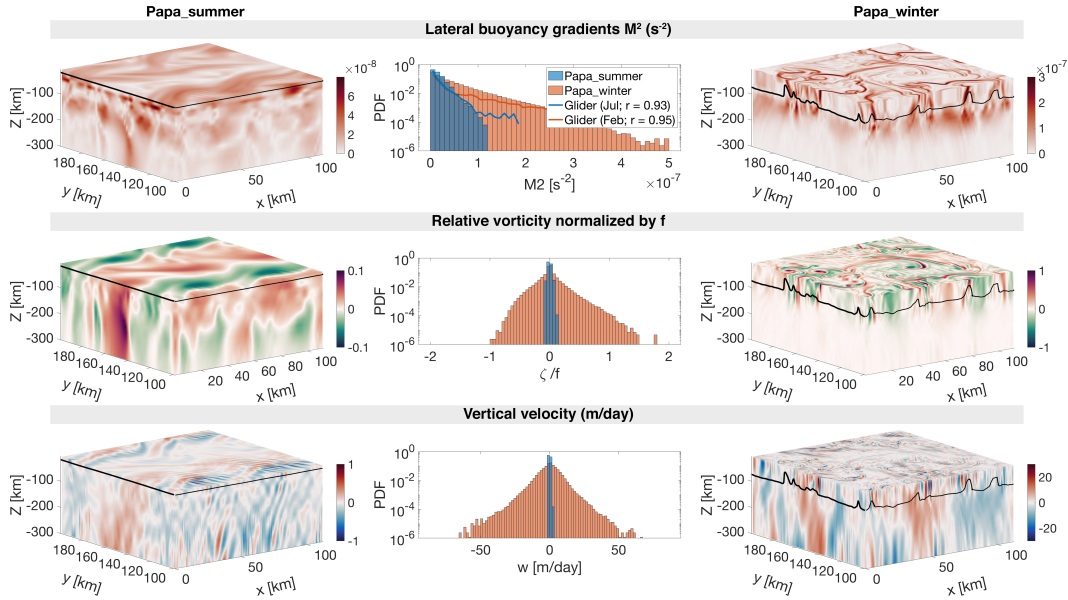
$$w_s(t) = w_s^0 \exp\left(-\frac{2kt}{3}\right), \quad (10)$$

where  $w_s^0$  is the initial sinking velocity at  $t = 0$  days. In this study, the impact of remineralization is thus considered through the implementation of a time-dependent sinking velocity (Equation 10). While particles classes are classified based on their initial sinking-velocity, it is worth noting that over the length of the particle-tracking experiments that include remineralization (28 days), particle sinking speeds slow down to 10% of their initial velocity.

## 3 Results

### 3.1 Seasonally varying dynamical regimes

Two model experiments are designed to capture different dynamical conditions observed in the Northeast Pacific Ocean in summer and winter. *Papa\_summer* is initialized in early spring (doy 105) when the water column is characterized by a relatively deep mixed layer ( $\sim 100$  m) and a halocline located between 100 and 150 m (Figure 2). The forcing by a realistic, positive, net heat flux generates the restratification of the water column, with the development of a strong thermocline between 25 and 50 m leading to the shoaling of the mixed layer and a subsurface peak in  $N^2$  at about 30 m (see Figure 2). A comparison between model outputs and monthly-averaged density



380 **Figure 5.** Snapshots of  $M^2$  (top),  $\zeta/f$  (middle), and  $w$  (bottom) half-way through the  
 381 particle tracking experiment for *Papa\_summer* (left) and *Papa\_winter* (right), with the Mixed  
 382 Layer Depth indicated by the solid black line. The corresponding Probability Distribution  
 383 Functions (PDFs) are shown in the center for both *Papa\_summer* (blue) and *Papa\_winter* (red). Note the  
 384 different colorbars used for *Papa\_summer* and *Papa\_winter*. Histograms of  $M^2$  computed from  
 385 glider data at Station Papa in February (blue line) and July (red line) are superimposed in the  
 386 top middle panel.

366 profiles from underwater gliders collected in June and July over the period 2008–2009  
 367 yields correlation coefficients of  $r = 0.87$  and  $r = 0.88$ , respectively. These high cor-  
 368 relation suggest that *Papa\_summer* numerical experiment captures the vertical spring  
 369 and summer conditions in the Northeast Pacific Ocean.

370 In the horizontal, the prescribed density fronts progressively become unstable  
 371 within the first 60 days of the experiment (Figure 2). During this time, the Total  
 372 Kinetic Energy ( $KE_{tot}$ ) contained in the model domain slowly increases before reach-  
 373 ing a maximum at doy 162, where it remains relatively constant for the rest of the  
 374 simulation. The flattening of the  $KE_{tot}$  curve is used to determine the time necessary  
 375 for the simulation to spin-up, hence determining the start day of the particle-tracking  
 376 experiments. The ocean dynamics associated with *Papa\_summer* are characterized  
 377 using PDFs of horizontal buoyancy gradients ( $M^2 = |\nabla_H b|^2$ ), vertical velocities ( $w$ ),  
 378 and Rossby numbers computed from the normalized vertical component of the relative  
 379 vorticity ( $Ro = (v_x - u_y)/f$  where  $f = 1.12 \times 10^{-4}$ ; Figure 5).

380 Lateral buoyancy gradients in the summer are relatively weak  $\mathcal{O}(10^{-8} \text{ s}^{-2})$  and  
 381 result in low Rossby numbers  $\mathcal{O}(0.1)$ , with positive relative vorticity on the denser  
 382 (north) side of the front and negative relative vorticity on the lighter (south) side  
 383 of the front. Corresponding vertical velocities are consistently weaker than 1 m/day  
 384 ( $< 10^{-5} \text{ m/s}$ ) and are characterized by regions of weak upwelling and downwelling on  
 385 10 km scales, associated with the meandering of the front (Bower & Rossby, 1989).  
 386 Alternating bands of upwelling and downwelling at  $\mathcal{O}(1 \text{ km})$  spatial scale are super-  
 387 imposed, and likely caused by propagating internal waves. Coherent vertical velocities  
 388 structures extend to depths much greater than the mixed layer depth ( $\sim 25 \text{ m}$ ; Figure  
 389

5). The amplitude of the vertical velocity field coincides with the expected order of magnitude given by the scaling  $w \propto Ro f U / N$  (Mahadevan, 2016): using  $Ro \sim 0.1$  (Figure 5),  $N \sim 10^{-2} \text{ s}^{-1}$  (Figure 2),  $f \sim 10^{-5} \text{ s}^{-1}$ , and  $U \sim 0.01 \text{ m/s}$ , we obtain  $w \sim 10^{-6} \text{ m/s}$ , or  $\sim 10^{-1} \text{ m/day}$ .

*Papa-winter* is, on the other hand, initialized in the winter (doy 0) to capture a time period where the mixed layer depth is deeper ( $\sim 100 \text{ m}$ ) and density gradients more pronounced (Pelland et al., 2016). At this time of year, the water column in this region is characterized by the presence of a deep halocline between 100 and 150 m (Figure 3 Pelland et al., 2016). After spin-up, the vertical stratification remains consistent throughout the model run, and compares well with the vertical profile obtained from glider observations for the month of March ( $r = 0.95$ ; see Figure 3). In the horizontal, prescribed density fronts are much sharper than in summer (i.e., over smaller spatial scales  $O(1 \text{ km})$  vs.  $O(10 \text{ km})$ ). Because of these stronger density gradients, combined with the alternating zonal winds and constantly negative surface heat flux, the fronts become unstable more rapidly than in summer (Figure 3). As a result,  $KE_{\text{tot}}$  starts to plateau at doy 48. The experiment is considered spun-up by doy 50 and the particle-tracking experiment is initialized.

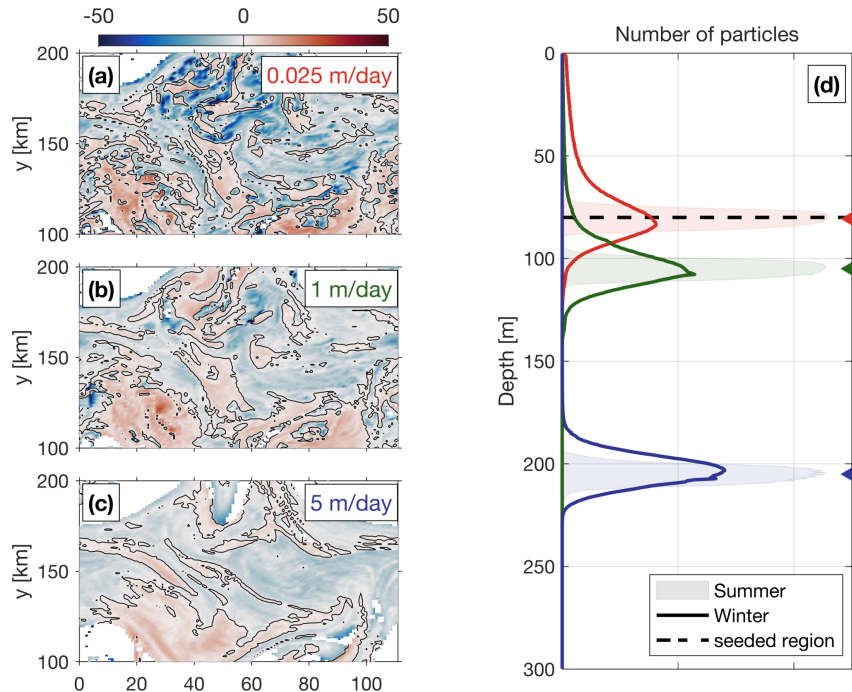
The frontal structures visible in the horizontal buoyancy gradient field are associated with filaments of relatively high Rossby number of  $O(1)$  (Figure 5). The PDF of relative vorticity reveals a positively-skewed distribution ( $s = 0.68$ ). This is in agreement with the fact that the relative vorticity is more likely to be cyclonic than anticyclonic, based on conservation of potential vorticity (Hoskins & Bretherton, 1972). Regions with high Rossby number are localized and located in the mixed layer exclusively. In places where the local Rossby number reaches  $O(1)$ , geostrophic balance is lost and a vertical secondary ageostrophic circulation begins to slump the isopycnals and restore the flow to a more geostrophically-balanced flow. This ageostrophic secondary circulation therefore generates “hot spots” of higher vertical velocities. The fine-scale structures in the vertical velocity field corresponding to  $O(1)$  Rossby numbers can be seen in Figure 5, with local vertical velocities up to  $60 \text{ m/day}$  ( $\sim 7 \times 10^{-4} \text{ m/s}$ ). Contrary to the PDF of relative vorticity, the distribution of vertical velocities demonstrate a negative skewness ( $s = -0.25$ ). This is in agreement with the theory: In fact, positive relative vorticity is associated with the dense side of a density front, where vertical velocities are negative (Mahadevan, 2016). Once again, the amplitude of these vertical velocity hot spots is coherent with the scaling  $w \propto Ro f U / N$ : using  $Ro \sim 1$ ,  $N \sim 10^{-2} \text{ 1/s}$ ,  $f \sim 10^{-5} \text{ 1/s}$ , and  $U \sim 0.1 \text{ m/s}$ , we obtain  $w \sim 10^{-4} \text{ m/s}$ , or  $\sim 10^1 \text{ m/day}$ .

Comparing *Papa-summer* and *Papa-winter* highlights the different dynamical regimes in the two experiments. In *Papa-winter*, density fronts tend to be sharper, meaning larger density gradients over shorter spatial scales. When computed at the kilometer-scale, the PDF of horizontal buoyancy gradients in *Papa-winter* exhibits a longer tail than in *Papa-summer* (Figure 5). When compared to observations, the PDFs of  $M^2$  in *Papa-summer* and *Papa-winter* demonstrate a correlation with observations of  $r = 0.93$  and  $r = 0.95$ , respectively.

The wider PDF of vertical velocities in *Papa-winter* shows advective velocities that match and exceed typical gravitational sinking velocities, particularly for smaller, and therefore slower-sinking, particulate organic material. The secondary ageostrophic circulation that develops at submeso-scales (i.e.,  $Ro O(1)$ ) therefore generates an export mechanism that directly competes with the traditional paradigm that relies on gravitational sinking leading the export of particulate matter in the ocean.

### 445 3.2 Gravitational and Advective Export of POC

446 Both model experiments described above were then used to investigate the re-  
 447 lationship between ocean dynamics and particle downward flux, using Lagrangian  
 448 particle-tracking. Domain-averaged, downward particle flux is expected to be a com-  
 449 bination of the flux driving by gravitational sinking ( $\langle w_s B \rangle$ ), and by the vertical ad-  
 450 vective currents affecting the particle along its pathway ( $\langle wB \rangle$ ). The deviation in  
 451 particle depths from the traditional one-dimensional gravitationally driven model is  
 452 shown in Figure 6 for both summer and winter cases. In the summer, the PDF of par-  
 453 ticle density versus depth remains relatively narrow through time, and is centered on  
 454 a depth level that can be predicted using a simple 1D gravitational model (see shaded  
 455 curves in Figure 6). The spread in the particle density also vary little among particle  
 456 classes with different sinking velocities, suggesting that downward fluxes of particles  
 457 is greatly dominated by gravitational settling and is not subject to significant vertical  
 458 ocean currents.



459 **Figure 6.** [left] The median depth anomaly of particles with a sinking speed (a) 0.025 m/d,  
 460 (b) 1 m/d, (c) 5 m/d within each grid cell for the winter case 25 days after particles are released.  
 461 The ‘depth anomaly’ is with respect to the ‘expected’ sinking depth (= sinking speed  $\times$  time  
 462 since release). Blue (red) grid cells indicate that the median depth of particles in this cell is  
 463 deeper (shallower) than expected, based on a 1D gravitational model where  $z = w_s \times t$ . [right] (d)  
 464 Probability Distribution Function (PDF) of particles as a function of depth for each velocity class  
 465  $c^2$  (red = 0.025 m/day; green = 1 m/day; blue = 5 m/day). The winter distribution is shown as  
 466 thick lines, while the summer distribution is represented by the shaded regions. Triangle markers  
 467 indicate the expected depth of particles after 25 days based on the 1D gravitational model, which  
 468 is used as a reference to compute the depth anomalies. Release depth is indicated by the thick  
 469 dashed line.

470 In the winter, however, PDFs of particle density versus depth is wider, in agree-  
 471 ment with the stronger vertical ocean currents occurring in the winter (see Figure 5).

472 A top-view of the deviation in the downward particle flux from the traditionally con-  
 473 sidered 1D gravitational model can be seen in Figure 6 (panels (a)-(c)). Slower-sinking  
 474 particles deviate more than faster-sinking particles, exhibiting median depth anom-  
 475 alies up to 50 m. This is due to the fact that slower-sinking particles spend more time  
 476 in the mixed layer, where most of the stronger vertical currents tend to occur (Figure  
 477 5). An interesting result emerges from the spatial distribution of the depth-anomaly:  
 478 both positive (i.e., particles are shallower than expected) and negative (i.e., particles  
 479 are deeper than expected) anomalies are organized into features with a length-scale  
 480  $\mathcal{O}(1\text{-}10 \text{ km})$ . This further highlights the importance of winter submesoscale circulation  
 481 for vertical fluxes of particles.

482 A relative amount of biomass is associated to the particles using Equation (8).  
 483 PDFs of relative biomass as a function of the vertical velocity is shown in Figure 7.  
 484 Following the traditional paradigm derived from the simple 1D gravitational model, the  
 485 downward flux of biomass in the summer is dominated by faster-sinking particle classes  
 486 capable of carrying particulate material downwards more efficiently. The contribution  
 487 of slower-sinking particles, however, depends critically on the slope of the size spectrum  
 488 (see Figure 4). As the Junge slope increases, the spectrum of biomass steepens, and  
 489 the relative contribution of slower-sinking particles to the downward biomass flux  
 490 significantly increases (Figure 7c). In fact, the contribution of slower-sinking particles  
 491 to the summer downward flux increases by a factor 100 (from 0.2% to  $\text{c}^1 0\%$ ) when the  
 492 Junge slope varies from  $\xi = 2$  to  $\xi = 4$ . While significant, the impact of a change in  
 493 the Junge slope in summer conditions does not challenge the dominant role played by  
 494 faster-sinking particles. This result can be explained by the fact that, in the summer,  
 495 vertical velocities are weak and vertical biomass fluxes are therefore gravitationally-  
 496 driven ( $\langle w_s B \rangle > \langle w B \rangle$ ).

504 In the winter, PDFs of relative biomass as a function of vertical velocities present  
 505 a much larger spread, with velocity magnitudes exceeding 50 m/day. For  $\xi = 2$ ,  
 506 the relative contribution of slower-sinking particles to the downward flux significantly  
 507 increases from 0.2% in the summer to about 3% in the winter, demonstrating the  
 508 impact advective velocities alone can have on vertical fluxes (Figure 7b). Nevertheless,  
 509 slower-sinking particles remain a relatively small contributor to the total downward  
 510 flux of biomass. When winter ocean dynamics are coupled with a steeper Junge slope,  
 511 however, slower-sinking particles largely dominate the downward biomass flux. In  
 512 our winter simulations with  $\xi = 4$ , we find that the slowest-sinking particle class is  
 513 responsible for about 79% of the biomass flux (Figure 7d).

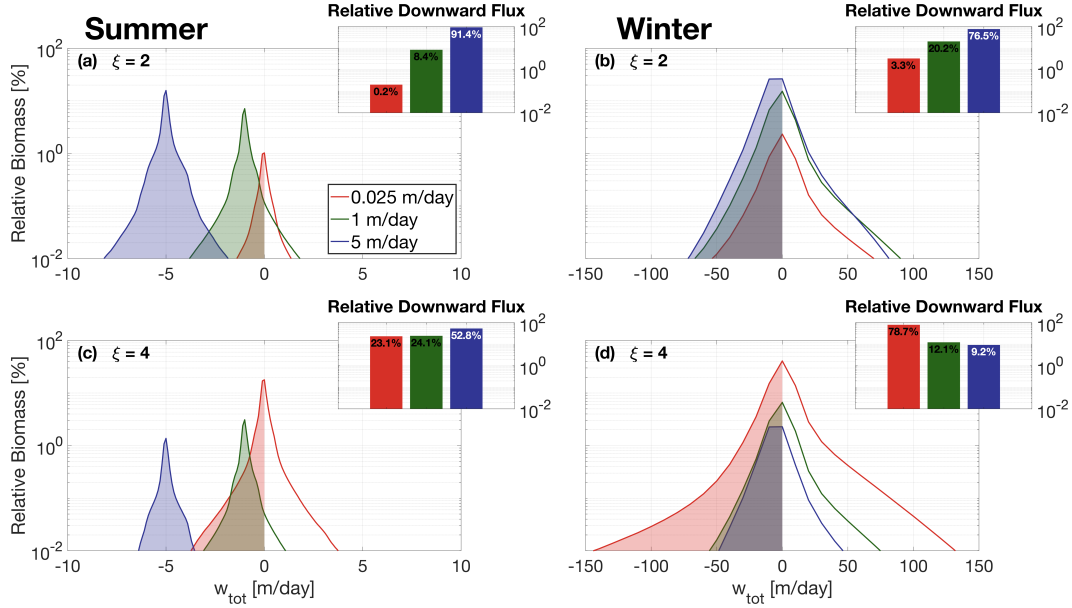
514 Our results show that both a steepening of the particle size spectrum and the  
 515 presence of submesoscale dynamics can enhance the contribution of slower-sinking par-  
 516 ticles to the downward biomass flux. While the former is simply due to an increase in  
 517 particle density in slower-sinking particle classes, the latter is attributed to the larger  
 518 vertical velocity generated by submesoscale instabilities. When both are combined,  
 519 as expected in the wintertime, slower-sinking particles then become the leading contrib-  
 520 utor to the downward biomass transport. However, slower-sinking particles are  
 521 generally expected to remineralize on timescales shorter than their export timescale,  
 522 fueling the argument that the focus should be upon faster-sinking particle classes. The  
 523 impacts of remineralization on export are thus considered in the following section to  
 524 test the robustness of the findings.

### 525 3.3 Particle Remineralization

526 Both submesoscale dynamics and the Junge slope were identified as key factors  
 527 impacting the respective role played by different particle classes in driving downward

---

c<sup>1</sup> 2



497 **Figure 7.** Probability Distribution Function (PDF) of relative biomass versus total vertical  
 498 velocity <sup>c5</sup>(sinking + advective) along particle trajectories in the summer case [left] and winter  
 499 case [right], with a Junge slope of 2 [top] and 4 [bottom]. <sup>c6</sup>PDFs are computed from the whole  
 500 24-day particle tracking experiments. Inserts show the integrated relative downward biomass flux  
 501 associated with each sinking-velocity class, categorized according to their initial sinking velocity  
 502 <sup>c7</sup>(red = 0.025 m/day; green = 1 m/day; blue = 5 m/day). Both winter dynamics and steeper  
 503 Junge slopes tend to increase the relative contribution of slower-sinking particles.

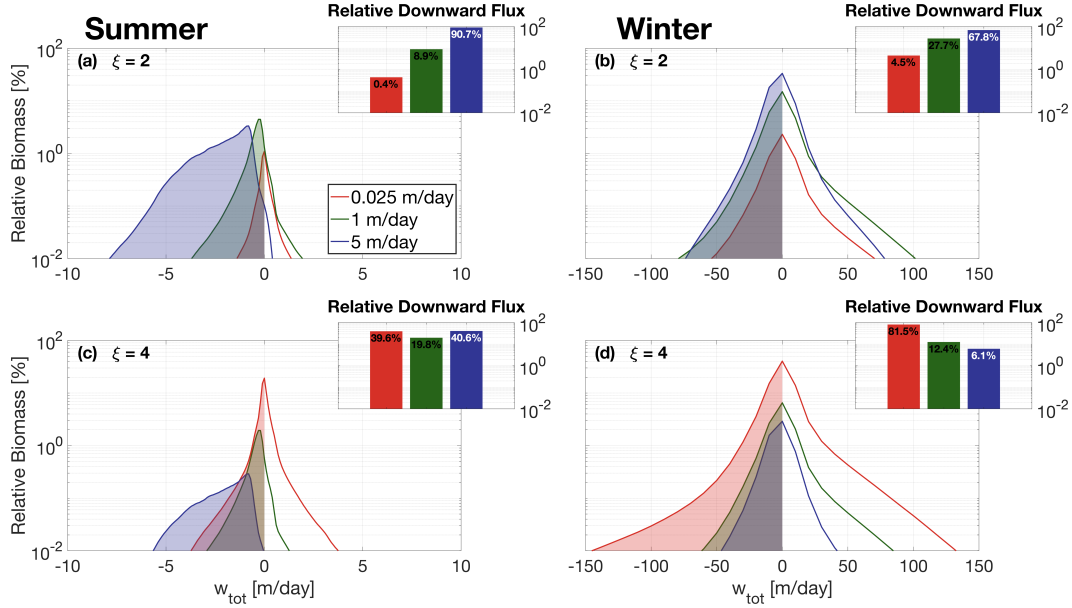
528 biomass fluxes. Simple Lagrangian particles were used to isolate the effects of these  
 529 two factors. In reality, however, sinking velocities of particulate matter varies in time  
 530 as the particles slowly remineralize. A remineralizing behavior was therefore imple-  
 531 mented for the Lagrangian particles, using Equation (10), to investigate the impact  
 532 that remineralization processes have on our findings. The traditional paradigm relies  
 533 on the fact that slow-sinking particles tend to fully remineralize over short timescales,  
 534 further enhancing the importance of faster-sinking particles classes in driving down-  
 535 ward biomass fluxes. While this paradigm holds for flatter Junge slope, where the  
 536 biomass content is dominated by faster-sinking particles, it becomes unfit at steeper  
 537 slopes.

538 Figure 8 compares the relative biomass and downward biomass fluxes associ-  
 539 ated with each of the modeled particle classes for <sup>c1</sup> $\xi = 2$  and  $\xi = 4$  <sup>c2</sup>including  
 540 the remineralization scheme. As previously detailed, downward fluxes of biomass  
 541 are dominated by faster-sinking particles during summertime and in the absence of  
 542 remineralization <sup>c3</sup>(see Figure 7). This is due to the fact that the flux of biomass  
 543  $\langle w_{tot}B \rangle = \langle w_s B \rangle + \langle w B \rangle$  is driven by  $\langle w_s B \rangle$ , despite a smaller relative biomass content  
 544 per particle. This is characteristic of a gravitationally-driven system, where settling  
 545 velocity dictates the contribution to downward fluxes. Implementing remineralization  
 546 processes, however, directly affects the particle settling velocity which slows down as

<sup>c1</sup> Text added.

<sup>c2</sup> with and without

<sup>c3</sup> Text added.



550 **Figure 8.** <sup>c3</sup>Same as Figure 7, but including particle remineralization (see Equation 10).

547 particles remineralize. This effect can <sup>c4</sup>particularly be seen in Figure 8<sup>c5</sup>a and c,  
548 where PDFs of relative biomass per particle class are shifted towards weaker vertical  
549 velocities than in the absence of remineralization, as predicted by Equation (10). <sup>c6</sup>

551 In an advectively-driven system where  $\langle w_s B \rangle \sim \langle w B \rangle$ , the relative amount of  
552 biomass content in a particle class becomes important and dictates the respective con-  
553 tribution of each particle class to the total downward biomass fluxes. This shift from a  
554 gravitationally-driven to an advectively-driven system is observed when implement-  
555 ing particle remineralization in the summer (Figure 8<sup>c5</sup>): in the absence of remineral-  
556 ization, faster-sinking particles dominate the downward biomass fluxes (<sup>c6</sup>53%; see  
557 Figure 7c). When remineralization processes are considered, slower-sinking particles  
558 <sup>c7</sup>contribute more to biomass fluxes (see inset in Figure 8c). As shown in Figure 7,  
559 downward biomass fluxes in the wintertime are generally advectively-driven, due to the  
560 larger vertical velocities associated with wintertime ocean dynamics. Biomass fluxes  
561 are dominated by the slower-sinking particles <sup>c8</sup>when  $\xi = 4$ , representing 79% of the  
562 downward biomass flux (Figure 7d). Even after implementing the remineralization  
563 scheme, slower-sinking particles remain the largest contributor to downward biomass  
564 fluxes (82%; see Figure 8d).

565 These results highlight the importance in considering slower-sinking particle  
566 classes when considering downward biomass fluxes. It also demonstrates that, con-  
567 trarily to the traditional paradigm, remineralization processes enhance the role played

<sup>c4</sup> Text added.

<sup>c5</sup> Text added.

<sup>c6</sup> As a result, the gravitationally-driven term  $\langle w_s B \rangle$  decreases with time, and the downward flux of  
biomass becomes generally advectively-driven by day 25 (Figure 8).

<sup>c5</sup> e

<sup>c6</sup> 60

<sup>c7</sup> become the dominant contributor

<sup>c8</sup> Text added.

568 by slower-sinking particles in biomass fluxes, in cases where the biomass spectrum  
 569 slope is negative.

## 570 4 Discussion

### 571 4.1 Dynamical Regimes

572 *Papa-summer* and *Papa-winter* experiments were designed to statistically cap-  
 573 ture the ocean dynamics at Station Papa (145°W, 50°N) in the Northeast Pacific  
 574 Ocean. After spin-up, the model demonstrated similar distributions of both horizontal  
 575 ( $M^2$ ) and vertical ( $N^2$ ) density gradients to observational estimates from underwater  
 576 gliders (see Figures 2, 3, and 5). The two experiments, however, show significantly  
 577 different distributions of  $M^2$ , with the winter distribution exhibiting a longer tail, due  
 578 to sharper density gradients. The tail of the wintertime distribution is only partially  
 579 captured by the glider data, due to the fact that underwater gliders sampled gradients  
 580 at spatial scales of 10 km and greater, while the model has a horizontal resolution of  
 581 500 m, allowing sharper submesoscale fronts and filaments to be formed.

582 Studies investigating submesoscale dynamics traditionally focused on regions  
 583 where the presence of submesoscale fronts and filaments are established, such as west-  
 584 ern boundary currents with strong gradients (D'Asaro, Lee, Rainville, Harcourt, &  
 585 Thomas, 2011; Thomas, Tandon, & Mahadevan, 2013), or the edge of mesoscale fea-  
 586 tures (van Haren et al., 2006; Waite et al., 2016). The seasonality in submesoscale  
 587 dynamics captured in the glider dataset at Station Papa and reflected in the model  
 588 experiments, echoes the behavior seen from recent observational studies conducted  
 589 at a similar latitude in the Atlantic Ocean, which demonstrate the intensification of  
 590 submesoscale dynamics in the wintertime (Buckingham et al., 2016; Thompson et al.,  
 591 2016). Despite being sometimes qualified as an “eddy desert” with low kinetic energy  
 592 (Chelton, Schlax, & Samelson, 2011), ocean characteristics in the eastern part of the  
 593 Pacific subpolar gyre suggest the presence of submesoscale features in the wintertime:  
 594 strong density gradients, localized Rossby numbers of order 1, a balanced Richardson  
 595 number  $Rib = \frac{f^2 N^2}{M^4}$  smaller than 1, a positively skewed distribution in vorticity, and a  
 596 negatively skewed distribution of vertical velocities (see Figure 5; Buckingham et al.,  
 597 2016; Rudnick, 2001; Thomas, Taylor, et al., 2013).

598 Strong downward velocities are hypothesized to enhance POC export by advect-  
 599 ing slower-sinking particles out of the mixed layer. *Papa-winter* indeed exhibits vertical  
 600 velocities more than 20 times larger than in *Papa-summer*. The vertical currents in  
 601 *Papa-winter*, however, tend to be much patchier than the weaker vertical currents  
 602 observed in *Papa-summer*. Because both particle production and downward vertical  
 603 velocities present a high degree of patchiness, it requires a certain level of covariance  
 604 between the two fields for the export to effectively be enhanced (Mahadevan et al.,  
 605 2012). A more realistic seeding strategy for Lagrangian particles, such as one guided  
 606 by biological tracers, would likely provide important information towards a better  
 607 understanding of the effects of patchiness on POC export at submeso-scales

608 The hypothesis tested in this study is that submesoscale activity enhances export  
 609 of particulate matter at Station Papa by shortening the export timescale of particulate  
 610 matter. The wintertime intensification in submesoscale activity has the potential to  
 611 indeed enhance export (see discussion in Section 4.2). However, the seasonal cycle  
 612 in submesoscale activity is out of phase with the one in net community productivity,  
 613 which peaks in the spring and summertime when the mixed layer is shallower (Plant  
 614 et al., 2016). Two mechanisms are therefore present to potentially sustain a year-long  
 615 POC export flux: In the winter, less particulate material is present in the mixed layer,  
 616 but active submesoscale dynamics tend to enhance the POC export flux by advecting  
 617 the more numerous slower-sinking particles into the ocean interior. In the summer,

618 the production of POC is at its yearly maximum, but export tends to be dominated  
 619 by gravitational sinking, which favors faster-sinking particles and thus exclude part of  
 620 the particle spectrum from contributing to the export flux.

## 621 4.2 Downward Fluxes

622 Analyses of particle tracking experiments reveal that the contribution of slower-  
 623 sinking particles to the downward particulate flux depends on two main factors: (1)  
 624 the dynamics of the oceanic flow field, and (2) the slope of the size spectrum (i.e., the  
 625 Junge slope  $\xi$ ).

626 Mixed layer ocean dynamics at station Papa change significantly between the  
 627 winter and the summer. In the winter, submesoscale dynamics are intensified, and  
 628 sharp fronts and filaments develop in the mixed layer. This seasonal change in dy-  
 629 namics is consistent with recent observations (Buckingham et al., 2016; Thompson  
 630 et al., 2016), and models (Brannigan, Marshall, Naveira-Garabato, & George Nurser,  
 631 2015; Callies et al., 2015; Rocha, Gille, Chereskin, & Menemenlis, 2016) characterizing  
 632 the seasonal cycle of submesoscale dynamics. The winter intensification in subme-  
 633 soscale dynamics was proven to have an important impact on the downward flux of all  
 634 sinking-velocity classes modeled in this experiment.

635 In the summer, gravitational sinking governs a downward particulate flux, which  
 636 is dominated by faster-sinking particles, with little to no contribution from slower-  
 637 sinking particles. In the winter, however, vertical fluxes tend to be advectively-driven,  
 638 which leads to a slightly weaker downward flux of faster-sinking particles than in the  
 639 summer due to resuspension, but a much larger flux of slower-sinking particles, which  
 640 are present in far greater numbers (Figure 7). The gravitationally-driven flux in the  
 641 summer is mechanistically different from the advectively-driven winter flux, which  
 642 raises the question as to which process is most efficient in driving a downward flux of  
 643 particulate material.

644 In the absence of remineralization, both a steeper size spectrum slope ( $\xi > 3$  in  
 645 this case) and enhanced submesoscale dynamics, increase the contribution of slower-  
 646 sinking particle classes to the downward biomass flux. This is only when both of  
 647 these conditions are combined, however, that slower-sinking particles dominate the  
 648 downward flux of biomass (Figure 7). This is a significant result, as Junge slopes  
 649 greater than 3 have been observed in the ocean <sup>c1</sup>: In-situ observations yield aver-  
 650 age spectral slopes varying between 3.5 and 4.5 (Kostadinov et al., 2009, see Table 2  
 651 in )<sup>c2</sup>, while spectral analysis of satellite data suggest global spectral slopes varying  
 652 between 3 and 6. More recent observational work located in the Northeast Pacific,  
 653 including Station Papa, found a spectral slope also greater than 3(White et al., 2015, ;  
 654 Z. Xiaodong, personal communication). <sup>c3</sup>Junge slopes are expected to vary in space,  
 655 depending on the community composition, both lateraly and vertically (Kostadinov  
 656 et al., 2009; White et al., 2015)<sup>c4</sup>, as well as in time; spectrum slopes tend to be flat-  
 657 ter during a spring bloom event, where larger particles (e.g., diatoms) are produced  
 658 in large quantities, and steeper during the wintertime, when communities are mostly  
 659 composed of small particles (Behrenfeld, 2010; Dale, Rey, & Heimdal, 1999; Parsons  
 660 & Lalli, 1988). The threshold value of  $\xi = 3$  for a change in the biomass spectral  
 661 slope (see Figure 4b) is of course a consequence of first-order approximations used  
 662 in this study describing the relationships between particle size, sinking velocity, and  
 663 biomass content. Nevertheless, our results demonstrate the importance of including the

---

<sup>c1</sup> *Text added.*

<sup>c2</sup> *Text added.*

<sup>c3</sup> *Text added.*

<sup>c4</sup> *Text added.*

664 smaller particle size range of the particle spectrum, in the estimation or measurement  
 665 of vertical fluxes, especially when submesoscale dynamics are active. It also highlights  
 666 the importance of better constraining the relationships linking particle size, sinking  
 667 velocity, and biomass content.

668 Introducing remineralization processes significantly decreases the biomass flux.  
 669 Counter-intuitively, however, the implementation of a remineralization scheme further  
 670 strengthens the contribution of slower-sinking particles to the biomass flux (Figure  
 671 8). This can be explained by the fact that remineralization processes have a greater  
 672 impact on sinking-velocity classes that rely on gravitational sinking to be exported, as  
 673 these particles decelerate as they remineralize. In the summer, all particle classes are  
 674 similarly affected by remineralization, as downward fluxes are gravitationally-driven.  
 675 In the winter, however, slower-sinking particles are exported through advective pro-  
 676 cesses. Their export timescale is barely affected by remineralization processes as it  
 677 only depends on local ocean dynamics.

678 <sup>c1</sup>These results are robust to the range of sinking rates explored. If one considers  
 679 a particle class with a sinking rate far exceeding the vertical advective velocity (e.g.,  
 680 100 m/day; Turner, 2015)<sup>c2</sup>, then the associated biomass flux can be estimated by  
 681 relying on the traditional 1-D paradigm, assuming  $w_{tot} \approx w_s$ . Combining this approx-  
 682 imation with Equation 8 shows that the slope of the biomass flux spectrum is positive  
 683 for  $\xi < 5$ , in which case very fast-sinking particles would dominate vertical biomass  
 684 fluxes. However, for  $\xi > 5$ , the slope of the biomass flux spectrum becomes negative  
 685 as well, meaning that the biomass flux is always dominated by the slow-sinking parti-  
 686 cle classes, regardless of the ocean dynamical regime. While considered large, values of  
 687  $\xi > 5$  remain realistic and fall within the range obtained from satellite-based estimates  
 688 (Kostadinov et al., 2009).

689 The results of this study suggest that slow- and non-sinking particles must be  
 690 considered when studying the downward flux of particulate matter in the upper ocean.  
 691 The patchiness associated with both particle production and submesoscale features  
 692 poses a real observational challenge to properly resolve vertical fluxes. Based on our  
 693 findings, subsequent studies should focus on testing the impact of patchiness on vertical  
 694 fluxes. In the wintertime, when size spectral slope is steep and submesoscale dynamics  
 695 most active, vertical fluxes could be grossly underestimated depending on the level of  
 696 co-occurrence between particle production and stronger vertical currents.

## 697 5 Conclusion

698 The main conclusions of this study are:

- 699 1. Ocean dynamics in the subpolar Northeast Pacific exhibit a seasonal cycle with  
 700 low submesoscale activity in the summertime, and more submesoscale features  
 701 present in the wintertime. Submesoscale dynamics generate larger, and asym-  
 702 metric, vertical currents leading to a vertical biomass flux driven by advective  
 703 processes, as opposed to gravitational sinking in the summertime.
- 704 2. Submesoscale dynamics generally enhance the downward particulate flux by  
 705 increasing the contribution of slower-sinking particles to the total flux through  
 706 advective transport. The slower-sinking particles are found to be significant  
 707 for export, and can be even make the dominant contribution under certain  
 708 conditions.

---

<sup>c1</sup> *Text added.*

<sup>c2</sup> *Text added.*

- 709        3. The contribution of slower-sinking particles to the downward biomass flux de-  
 710        pends on the slope of the particle size spectra (i.e., the Junge Slope), that  
 711        controls the relative number of particles per size class. Two cases emerge from  
 712        this study:
- 713        (a) If the Junge slope is smaller than 3, larger particles contribute most to vertical  
 714        biomass fluxes independently of flow dynamics, as there are no mechanisms  
 715        capable of selectively advecting slower-sinking particles. The system is de-  
 716        scribed as gravitationally-driven.
- 717        (b) If the Junge slope is greater than 3, as most commonly observed, ocean  
 718        dynamics become key for determining which particle classes dominate the  
 719        downward flux. As submesoscale dynamics become more active, ageostrophic  
 720        circulations leading to larger vertical velocities develop. In these conditions,  
 721        downward biomass fluxes are largely driven by the slower-sinking particle  
 722        classes.
- 723        4. Remineralization processes logically reduce the amount of biomass flux. How-  
 724        ever, it unexpectedly enhances the role of slower-sinking particles, which are are  
 725        advectively transported. The impact of remineralization is greater on faster-  
 726        sinking particles since it affects both the biomass content and their sinking  
 727        velocity.

728        **Acknowledgments**

729        The work was funded by NASA grant NNX16AR48G, to complement the EXport  
 730        Processes in the global Ocean from RemoTe Sensing (EXPORTS) program. We would  
 731        like to thank A. Thompson (Caltech) for his useful comments and suggestions, N.  
 732        Pelland (NOAA) and C. Eriksen (University of Washington) for sharing the glider data  
 733        collected at Ocean Station Papa, as well as S. Essink for his assistance in developing the  
 734        particle-tracking code. All data used in this manuscript are publicly available: Ocean  
 735        Station Papa data is available on PMEL's website (<https://www.pmel.noaa.gov/ocs/Papa>; PMEL, 2018) and gridded Argo products can be downloaded at <http://www.seanoe.org/data/00348/45945> (Gaillard, 2015). Glider data is archived at the  
 736        University of Washington's Library (<http://hdl.handle.net/1773/41656>; Pelland,  
 737        2018). Code to reproduce analysis and figures are publicly available at [https://github.com/matdever/Size-differentiated\\_Export\\_GBC](https://github.com/matdever/Size-differentiated_Export_GBC) (Dever, 2020). Due to the  
 738        very large filesize, model outputs and particle trajectories are available on request.

742        **References**

- 743        Alkire, M., D'Asaro, E., Lee, C., Perry, M., Gray, A., Cetinic, I., ... González-  
 744        Posada, A. (2012). Estimates of net community production and export using  
 745        high-resolution, Lagrangian measurements of O<sub>2</sub>, NO<sub>3</sub><sup>-</sup>, and POC through the  
 746        evolution of a spring diatom bloom in the North Atlantic. *Deep-Sea Res. I*,  
 747        64, 157-174. doi: 10.1016/j.dsr.2012.01.012
- 748        Bach, L. T., Riebesell, U., Sett, S., Febiri, S., Rzepka, P., & Schulz, K. G. (2012).  
 749        An approach for particle sinking velocity measurements in the 3–400 μm size  
 750        range and considerations on the effect of temperature on sinking rates. *Marine  
 751        Biology*, 159(8), 1853–1864. doi: 10.1007/s00227-012-1945-2
- 752        Behrenfeld, M. J. (2010). Abandoning sverdrup's critical depth hypothesis on phyto-  
 753        plankton blooms. *Ecology*, 91(4), 977-989. doi: 10.1890/09-1207.1
- 754        Bower, A. S., & Rossby, T. (1989). Evidence of Cross-Frontal Exchange Processes  
 755        in the Gulf Stream Based on Isopycnal RAFOS Float Data. *Journal of Phys-  
 756        ical Oceanography*, 19(9), 1177–1190. doi: 10.1175/1520-0485(1989)019<1177:  
 757        EOCFEP>2.0.CO;2

- 758 Brannigan, L., Marshall, D. P., Naveira-Garabato, A., & George Nurser, A. (2015).  
 759 The seasonal cycle of submesoscale flows. *Ocean Modelling*, 92, 69–84. doi: 10  
 760 .1016/j.ocemod.2015.05.002
- 761 Briggs, N., Perry, M. J., Cetinić, I., Lee, C., D’Asaro, E., Gray, A. M., & Rehm, E.  
 762 (2011). High-resolution observations of aggregate flux during a sub-polar north  
 763 atlantic spring bloom. *Deep Sea Research Part I: Oceanographic Research  
 764 Papers*, 58(10), 1031 - 1039. doi: 10.1016/j.dsr.2011.07.007
- 765 Buckingham, C. E., Naveira Garabato, A. C., Thompson, A. F., Brannigan, L.,  
 766 Lazar, A., Marshall, D. P., ... Belcher, S. E. (2016). Seasonality of sub-  
 767 mesoscale flows in the ocean surface boundary layer. *Geophysical Research  
 768 Letters*, 43(5), 2118–2126. doi: 10.1002/2016GL068009
- 769 Callies, J., Ferrari, R., Klymak, J. M., & Gula, J. (2015). Seasonality in sub-  
 770 mesoscale turbulence. *Nature communications*, 6, 6862. doi: 10.1038/  
 771 ncomms7862
- 772 Chelton, D. B., Schlax, M. G., & Samelson, R. M. (2011). Global observations of  
 773 nonlinear mesoscale eddies. *Progress in Oceanography*, 91(2), 167–216. doi: 10  
 774 .1016/j.pocean.2011.01.002
- 775 Dale, T., Rey, F., & Heimdal, B. R. (1999). Seasonal development of phytoplankton  
 776 at a high latitude oceanic site. *Sarsia*, 84(5-6), 419-435. doi: 10.1080/00364827  
 777 .1999.10807347
- 778 D’Asaro, E., Lee, C., Rainville, L., Harcourt, R., & Thomas, L. (2011). Enhanced  
 779 turbulence and energy dissipation at ocean fronts. *Science*, 332(6027), 318–  
 780 322. doi: 10.1126/science.1201515
- 781 Dever, M. (2020). *Size differentiated Export GBC: Release 1.* (data retrived from  
 782 GitHub, [https://github.com/matdever/Size-differentiated\\_Export\\_GBC](https://github.com/matdever/Size-differentiated_Export_GBC))  
 783 doi: 10.5281/zenodo.3908126
- 784 Döös, K., Kjellsson, J., & Jönsson, B. (2013). TRACMASS – A Lagrangian Trajec-  
 785 tory Model. In *Preventive methods for coastal protection* (pp. 225–249). Heidel-  
 786 berg: Springer International Publishing. doi: 10.1007/978-3-319-00440-2\_7
- 787 Ducklow, H. W., Steinberg, D. K., & Buesseler, K. O. (2001). Upper Ocean Carbon  
 788 Export and the Biological Pump. *Oceanography*, 14. doi: <https://doi.org/10.5670/oceanog.2001.06>
- 789 Estapa, M. L., Siegel, D. A., Buesseler, K. O., Stanley, R. H. R., Lomas, M. W., &  
 790 Nelson, N. B. (2015). Decoupling of net community and export production  
 791 on submesoscales in the Sargasso Sea. *Global Biogeochemical Cycles*, 29(8),  
 792 1266–1282. doi: 10.1002/2014GB004913
- 793 Falkowski, P. G., Barber, R. T., & Smetacek, V. (1998). Biogeochemical Controls  
 794 and Feedbacks on Ocean Primary Production. *Science*, 281(5374), 200–206.  
 795 doi: 10.1126/science.281.5374.200
- 796 Fox-Kemper, B., Ferrari, R., & Hallberg, R. (2008). Parameterization of Mixed  
 797 Layer Eddies. Part I: Theory and Diagnosis. *Journal of Physical Oceanogra-  
 798 phy*, 38(6), 1145–1165. doi: 10.1175/2007JPO3792.1
- 799 Gaillard, F. (2015). *ISAS-13 temperature and salinity gridded fields. SEANOE*. doi:  
 800 10.17882/45945
- 801 Gaillard, F., Reynaud, T., Thierry, V., Kolodziejczyk, N., & von Schuckmann, K.  
 802 (2016). In situ-based reanalysis of the global ocean temperature and salinity  
 803 with isas: Variability of the heat content and steric height. *Journal of Climate*,  
 804 29(4), 1305-1323. doi: 10.1175/JCLI-D-15-0028.1
- 805 Gruber, N., Lachkar, Z., Frenzel, H., Marchesiello, P., Münnich, M., McWilliams,  
 806 J. C., ... Plattner, G.-K. (2011). Eddy-induced reduction of biological pro-  
 807 duction in eastern boundary upwelling systems. *Nature geoscience*, 4(11), 787.  
 808 doi: 10.1038/NGEO1273
- 809 Harrison, P. J., Whitney, F. A., Tsuda, A., Saito, H., & Tadokoro, K. (2004).  
 810 Nutrient and Plankton Dynamics in the NE and NW Gyres of the Sub-  
 811 arctic Pacific Ocean. *Journal of Oceanography*, 60(1), 93–117. doi:  
 812

- 813 10.1023/B:JOCE.0000038321.57391.2a  
 814 Hoskins, B. J., & Bretherton, F. P. (1972). Atmospheric Frontogenesis Models:  
 815 Mathematical Formulation and Solution. *Journal of the Atmospheric Sciences*,  
 816 29(1), 11–37. doi: 10.1175/1520-0469(1972)029<0011:AFMMFA>2.0.CO;2  
 817 Iversen, M. H., & Ploug, H. (2010). Ballast minerals and the sinking carbon flux in  
 818 the ocean: carbon-specific respiration rates and sinking velocity of marine snow  
 819 aggregates. *Biogeosciences*, 7(9), 2613–2624. doi: 10.5194/bg-7-2613-2010  
 820 Iversen, M. H., & Ploug, H. (2013). Temperature effects on carbon-specific respi-  
 821 ration rate and sinking velocity of diatom aggregates - potential implications  
 822 for deep ocean export processes. *Biogeosciences*, 10(6), 4073–4085. doi:  
 823 10.5194/bg-10-4073-2013  
 824 Klein, P., & Lapeyre, G. (2009). The Oceanic Vertical Pump Induced by Mesoscale  
 825 and Submesoscale Turbulence. *Annual Review of Marine Science*, 1(1), 351–  
 826 375. doi: 10.1146/annurev.marine.010908.163704  
 827 Kostadinov, T. S., Siegel, D. A., & Maritorena, S. (2009). Retrieval of the particle  
 828 size distribution from satellite ocean color observations. *Journal of Geophysical  
 829 Research*, 114(C9), C09015. doi: 10.1029/2009JC005303  
 830 Lévy, M., Ferrari, R., Franks, P. J. S., Martin, A. P., & Rivière, P. (2012). Bringing  
 831 physics to life at the submesoscale. *Geophysical Research Letters*, 39(14), n/a–  
 832 n/a. doi: 10.1029/2012GL052756  
 833 Lévy, M., Klein, P., & Treguier, A.-M. (2001). Impact of sub-mesoscale physics on  
 834 production and subduction of phytoplankton in an oligotrophic regime. *Jour-  
 835 nal of marine research*, 59(4), 535–565. doi: 10.1357/002224001762842181  
 836 Mahadevan, A. (2016). The Impact of Submesoscale Physics on Primary Produc-  
 837 tivity of Plankton. *Annual Review of Marine Science*, 8(1), 161–184. doi: 10  
 838 .1146/annurev-marine-010814-015912  
 839 Mahadevan, A., & Archer, D. (2000). Modeling the impact of fronts and  
 840 mesoscale circulation on the nutrient supply and biogeochemistry of the up-  
 841 per ocean. *Journal of Geophysical Research: Oceans*, 105(C1), 1209–1225. doi:  
 842 10.1029/1999JC900216  
 843 Mahadevan, A., D'Asaro, E., Lee, C., & Perry, M. J. (2012). Eddy-Driven Strat-  
 844 ification Initiates North Atlantic Spring Phytoplankton Blooms. *Science*,  
 845 337(6090), 54–58. doi: 10.1126/science.1218740  
 846 Mahadevan, A., Oliger, J., & Street, R. (1996a). A Nonhydrostatic Mesoscale Ocean  
 847 Model. Part II: Numerical Implementation. *Journal of Physical Oceanography*,  
 848 26(9), 1881–1900. doi: 10.1175/1520-0485(1996)026<1881:ANMOMP>2.0.CO;  
 849 2  
 850 Mahadevan, A., Oliger, J., & Street, R. (1996b). A Nonhydrostatic mesoscale ocean  
 851 model. Part I: Well-posedness and scaling. *Journal of Physical Oceanography*,  
 852 26(9), 1868–1880. doi: 10.1175/1520-0485(1996)026<1868:ANMOMP>2.0.CO;  
 853 2  
 854 Mahadevan, A., & Tandon, A. (2006). An analysis of mechanisms for submesoscale  
 855 vertical motion at ocean fronts. *Ocean Modelling*, 14(3-4), 241–256. doi: 10  
 856 .1016/J.OCEMOD.2006.05.006  
 857 McDonnell, A. M. P., & Buesseler, K. O. (2010). Variability in the average sinking  
 858 velocity of marine particles. *Limnology and Oceanography*, 55(5), 2085–2096.  
 859 doi: 10.4319/lo.2010.55.5.2085  
 860 McWilliams, J. C. (2016). Submesoscale currents in the ocean. *Proceedings of the  
 861 Royal Society A: Mathematical, Physical and Engineering Science*, 472(2189).  
 862 doi: 10.1098/rspa.2016.0117  
 863 Mensa, J. A., Garraffo, Z., Griffa, A., Özgökmen, T. M., Haza, A., & Veneziani, M.  
 864 (2013). Seasonality of the submesoscale dynamics in the Gulf Stream region.  
 865 *Ocean Dynamics*, 63(8), 923–941. doi: 10.1007/s10236-013-0633-1  
 866 Mesinger, F., DiMego, G., Kalnay, E., Mitchell, K., Shafran, P. C., Ebisuzaki, W.,  
 867 ... Shi, W. (2006). North american regional reanalysis. *Bulletin of the Ameri-*

- can Meteorological Society, 87(3), 343–360. doi: 10.1175/BAMS-87-3-343
- Omand, M. M., D’Asaro, E. A., Lee, C. M., Perry, M. J., Briggs, N., Cetini, I., & Mahadevan, A. (2015). Eddy-driven subduction exports particulate organic carbon from the spring bloom. *Science*, 348(6231), 222–225. doi: 10.1126/science.1260062
- Parsons, T. R., & Lalli, C. M. (1988). Comparative oceanic ecology of the plankton communities of the subarctic Atlantic and Pacific oceans. *Oceanography and Marine Biology Annual Review*, 26, 317–359.
- Pelland, N. (2018). *Seaglider Surveys at Ocean Station Papa: Bin-Averaged Profiles, Currents, and Independent Oxygen Data*. Retrieved from <http://hdl.handle.net/1773/41656>
- Pelland, N., Eriksen, C., & Cronin, M. (2016). Seaglider surveys at Ocean Station Papa: Circulation and watermass properties in a meander of the North Pacific Current. *Journal of Geophysical Research: Oceans*, 121, 6816–6846. doi: 10.1002/2016JC011920
- Plant, J. N., Johnson, K. S., Sakamoto, C. M., Jannasch, H. W., Coletti, L. J., Riser, S. C., & Swift, D. D. (2016). Net community production at Ocean Station Papa observed with nitrate and oxygen sensors on profiling floats. *Global Biogeochemical Cycles*, 30(6), 859–879. doi: 10.1002/2015GB005349
- Ploug, H., Iversen, M. H., Koski, M., & Buitenhuis, E. T. (2008). Production, oxygen respiration rates, and sinking velocity of copepod fecal pellets: Direct measurements of ballasting by opal and calcite. *Limnology and Oceanography*, 53(2), 469–476. doi: 10.4319/lo.2008.53.2.0469
- PMEL. (2018). *Pacific Marine Environment Laboratory Ocean Climate Stations Mooring Data*. Retrieved from <https://www.pmel.noaa.gov/ocs/data-overview>
- Rocha, C. B., Gillett, S. T., Chereskin, T. K., & Menemenlis, D. (2016). Seasonality of submesoscale dynamics in the Kuroshio Extension. *Geophysical Research Letters*, 43(21), 11,304–11,311. doi: 10.1002/2016GL071349
- Rudnick, D. L. (2001). On the skewness of vorticity in the upper ocean. *Geophysical Research Letters*, 28(10), 2045–2048. doi: 10.1029/2000GL012265
- Sheldon, R., Prakash, A., & Sutcliffe, W., Jr. (1972). The size distribution of particles in the ocean. *Limnology and Oceanography*, 17(3), 327–340. doi: 10.4319/lo.1972.17.3.0327
- Sherry, N. D., Boyd, P. W., Sugimoto, K., & Harrison, P. J. (1999). Seasonal and spatial patterns of heterotrophic bacterial production, respiration, and biomass in the subarctic NE Pacific. *Deep-Sea Research Part II: Topical Studies in Oceanography*, 46(11–12), 2557–2578. doi: 10.1016/S0967-0645(99)00076-4
- Thomas, L. N., Tandon, A., & Mahadevan, A. (2013). Submesoscale processes and dynamics. In *Ocean modeling in an eddying regime* (p. 17–38). American Geophysical Union (AGU). doi: 10.1029/177GM04
- Thomas, L. N., Taylor, J. R., Ferrari, R., & Joyce, T. M. (2013). Symmetric instability in the Gulf Stream. *Deep Sea Research Part II: Topical Studies in Oceanography*, 91, 96–110. doi: 10.1016/j.dsr2.2013.02.025
- Thompson, A. F., Lazar, A., Buckingham, C., Naveira Garabato, A. C., Damerell, G. M., & Heywood, K. J. (2016). Open-Ocean Submesoscale Motions: A Full Seasonal Cycle of Mixed Layer Instabilities from Gliders. *Journal of Physical Oceanography*, 46(4), 1285–1307. doi: 10.1175/JPO-D-15-0170.1
- Turner, J. T. (2015). Zooplankton fecal pellets, marine snow, phytodetritus and the ocean’s biological pump. *Progress in Oceanography*, 130, 205–248.
- van Haren, H., Millot, C., & Taupier-Letage, I. (2006). Fast deep sinking in Mediterranean eddies. *Geophysical Research Letters*, 33(4), L04606. doi: 10.1029/2005GL025367
- Waite, A. M., Stemmann, L., Guidi, L., Calil, P. H. R., Hogg, A. M. C., Feng, M., ... Gorsky, G. (2016). The wineglass effect shapes particle export to the deep

- 923 ocean in mesoscale eddies. *Geophysical Research Letters*, 43(18), 9791–9800.  
924 doi: 10.1002/2015GL066463
- 925 White, A. E., Letelier, R. M., Whitmire, A. L., Barone, B., Bidigare, R. R., Church,  
926 M. J., & Karl, D. M. (2015). Phenology of particle size distributions  
927 and primary productivity in the North Pacific subtropical gyre (Station  
928 ALOHA). *Journal of Geophysical Research: Oceans*, 120(11), 7381–7399.  
929 doi: 10.1002/2015JC010897